High Step-Up Y-Source Inverter With Reduced DC-Link Voltage Spikes

Hongpeng Liu, *Member, IEEE*, Zichao Zhou, Kuan Liu, Poh Chiang Loh, Wei Wang, *Member, IEEE*, Dianguo Xu, *Fellow, IEEE*, and Frede Blaabjerg, *Fellow, IEEE*

***Abstract*—Impedance-source inverters using coupled inductors have been investigated as alternatives for providing high step-up voltages. However, leakage inductances of the coupled inductors have commonly led to lower overall effectiveness, in addition to generating high dc-link voltage spikes. The latter raises voltage stresses of switches, which in turn, may reduce the power levels of the inverters. A high step-up Y-source inverter has therefore been proposed in this paper to provide a high boost with a smooth dc-link voltage ensured by proper recycling of the leakage energy. These features have been verified by comparing simulation and experimental results of an existing Y-source and the proposed inverters. Factors compared are their respective boost ratios, voltage stresses, current stresses, and dc-link voltage spikes.**

***Index Terms*—Impedance-source inverter, leakage and coupled inductances, voltage spikes, Y-source inverters (YSI).**

I. Introduction

TRADITIONAL voltage-source inverters and current-source inverters have some drawbacks, such as their limited load voltage and/or current ranges, and output distortions due to deadtimes or overlap delays. These issues have subsequently led to the development of impedance-source inverters, which can both buck and boost voltages without demanding for deadtimes or overlap delays. The most representative of which is the Z-source voltage-type inverter [1], whose two switches from the same phase-leg can be turned ON simultaneously for a short shoot-through (ST) duration. It is thus less affected by unintentional short-circuit and waveform distortion, while providing the necessary voltage boost and buck.

Some improvements can however still be introduced to the Z-source inverter, which gradually lead to other developments. One of them is the quasi-Z-source inverter, proposed in [2], for realizing continuous input current. Others can be found in [3]–[7], where the switched-inductor and switched-capacitor techniques have been added for achieving higher gains with the same specified ST duration or duty ratio. However, more inductors or capacitors, and diodes are needed, and hence not so appealing in practice. The same applies to the extended-boost Z-source inverters found in [8]–[11], where more stages have been added for even higher gains.

Manuscript received April 5, 2018; revised July 11, 2018; accepted August 15, 2018. Date of publication August 21, 2018; date of current version April 20, 2019. This work was supported by the National Key R&D Program of China under Grant 2016YFE0102800. Recommended for publication by Associate Editor D. Vinnikov. *(Corresponding author: Hongpeng Liu.)*

H. Liu, Z. Zhou, K. Liu, W. Wang, and D. Xu are with the Department of Electrical Engineering, Harbin Institute of Technology, Harbin 150001, China (e-mail:

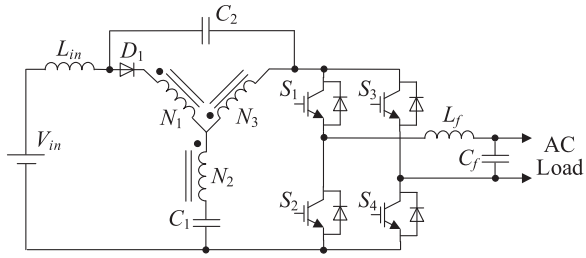

Fig. 1. Improved Y-source inverter.

An attempt to reduce components without compromising gains has then been started, leading to various impedance-source networks with coupled inductors, rather than numerous discrete components [12]–[17]. High voltage gains can now be achieved by altering turns ratios of the coupled inductors, even with only small ST duty ratios used. Despite that, some problems remain, like the sourcing of pulsed input currents, which can obviously be solved by adding inductors and/or capacitors for filtering. An example can be found in Fig. 1, where L_{in} and C_2 have been added to the original Y-source inverter (YSI) with a three-winding coupled inductor (N_1, N_2 and N_3). A gradual start-up and a smoother input current can then be enforced by L_{in}, whose current will continue to flow through C_2, whenever D_1 blocks. The resulting inverter has hence been referred to as the improved YSI (I-YSI) [18], [19].

It should however be clarified that pulsed input current is not uniquely related to the coupled inductor, since it has also been experienced by the original Z-source inverter. Rather, the coupled inductor may cause large voltage spikes at the dc-link when currents through its leakage inductances undergo rapid interruptions. This may happen when the inverter switches from ST to non-ST (NST) state and may undesirably lead to higher rated switches needed for realization. It is thus not practical to consider most existing impedance-source inverters with coupled inductors, unless appropriate absorbing circuits are introduced to them for preventing the voltage spikes.

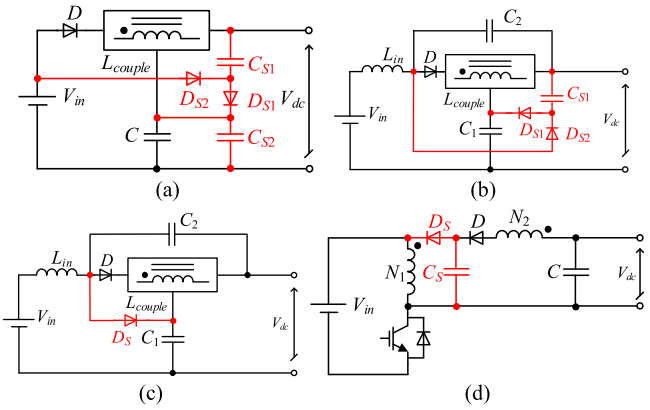

Fig. 2. Illustration of passive absorbing. (a) Circuit 1 [20]. (b) Circuit 2 [21]. (c) Circuit 3 [22]. (d) Circuit 4 [23].

To date, absorbing circuits can either be active or passive, whose common purpose is to provide a path for the leakage energy to flow. This is important, since regardless of the cores and winding techniques adopted, leakage inductances cannot be nullified completely. An absorbing circuit for continuously recycling the leakage energy to the source or capacitor is thus necessary, which in [20], is implemented by an extra dc–dc buck converter. This solution may however be complex and costly, because of the extra switch, and its accompanied control and driving circuits. Passive absorbing circuits without extra switches have therefore been introduced. Some possible circuits with different types and numbers of extra components are shown in Fig. 2 (in red), where their coupled inductors L_{couple} can have either two or three windings. Their respective operating principles vary slightly, even though their common purpose is to suppress the dc-link voltage spikes.

For instance, the circuit in Fig. 2(a) relies on capacitors and diode for clamping the dc-link voltage [20], but may experience damaging large current drawn from the power source at the instant of entering the ST state. This large current will, in fact, flow through diode $D_{\text{S}2}$, capacitor $C_{\text{S}1}$, and the shorted phase-leg, before returning to the power source with no limiting inductance in the loop. The current is thus momentarily large and may sometimes damage semiconductor devices unintentionally. A better alternative may then be the second passive absorbing circuit shown in Fig. 2(b) [21], where diode $D_{\text{S}2}$ conducts only when voltage of capacitor $C_{\text{S}1}$ becomes greater than that of C_2. On the other hand, diode $D_{\text{S}1}$ conducts only during the transfer from ST to NST state, which together with $C_{\text{S}1}$ and C_1, will clamp the otherwise spiky dc-link voltage.

The same effect may also be achieved by the simplified absorbing circuit shown in Fig. 2(c) [22], where the conduction of diode D_{S} connects C_1 and C_2 in series across the dc-link for limiting its voltage. The main drawback with Fig. 2(c), and also Fig. 2(b), is that their absorbing circuits can only be used with the I-YSI in Fig. 1 or other inverters with the same configuration but different number of coupled windings. Such restriction of usage is even more severe with the absorbing circuit shown in Fig. 2(d), comprising diode D_{S} and capacitor C_{S}. No doubt, this absorbing circuit has earlier been used with a popular

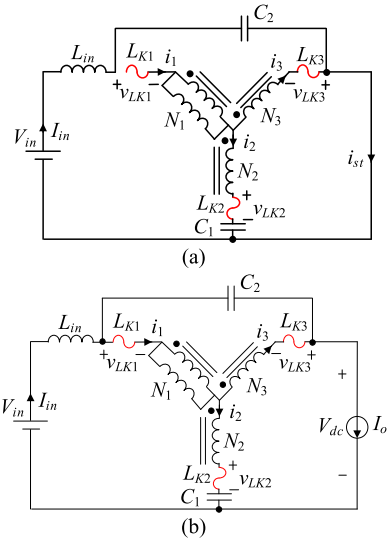

Fig. 3. Equivalent circuits of I-YSI when in (a) ST and (b) NST states.

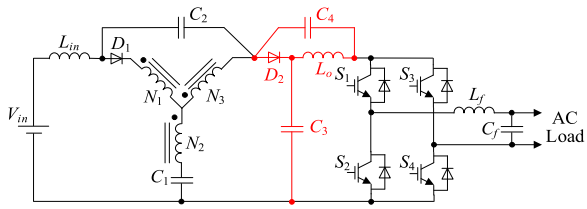

Fig. 4. High step-up Y-source inverter.

high-efficiency high-step-up converter [23], but its extension to an impedance-source inverter with a coupled inductor is generally not so viable. It is therefore not an option for consideration.

Another technique investigated in [24] is to reorient the three coupled windings shown in Fig. 1 from Y to Δ without introducing an absorbing circuit. The purpose is to lower the equivalent leakage inductances and equivalent series resistances (ESRs) of the windings, but by doing so, the number of turns of the third winding can no longer be decided independently. It is thus no different from a coupled inductor with only two windings, in terms of achievable voltage gains. Moreover, since some leakage inductances still remain, a Δ-connected coupled inductor may not help greatly with the subduing of dc-link voltage spikes, if an absorbing circuit has not been added.

Therefore, in this paper, a more effective absorbing circuit has been proposed for eliminating dc-link voltage spikes and improving the overall boost ability. The proposed circuit consists of two capacitors, one diode and one inductor, which when merged with the I-YSI in Fig. 1, yield a high step-up YSI (HS-YSI) with low dc-link voltage spikes.

II. Leakage Effects From Coupled Inductor

In most impedance-source inverters with coupled inductors, leakage inductances may reduce gain, lower efficiency, and generate dc-link voltage spikes. The generated voltage spikes may sometimes be larger than the normal dc-link voltage, which certainly, is a critical concern. How and when these spikes are generated should hence be explained first, before describing the

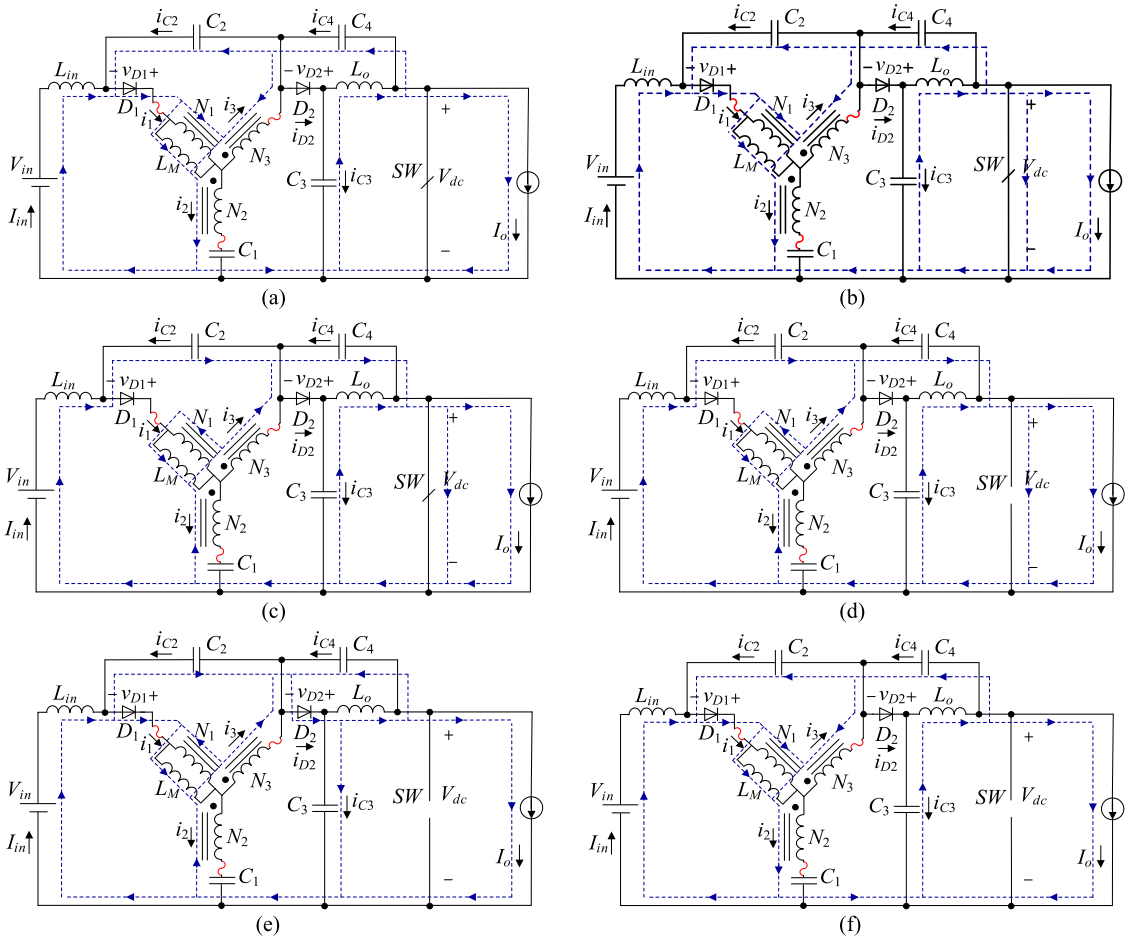

Fig. 5. Operational modes of HS-YSI when in (a) $[t_0, t_1]$, (b) $[t_1, t_2]$, (c) $[t_2, t_3]$, (d) $[t_3, t_4]$, (e) $[t_4, t_5]$, and (f) $[t_5, t_0]$.

proposed HS-YSI. For the explanation, the I-YSI in Fig. 1 is considered. Its equivalent circuits in both ST and NST states are shown in Fig. 3, where leakage inductances (in red) of three windings have been marked as L_{K1}, L_{K2}, and L_{K3}.

Assuming now that the I-YSI is initially in its ST state in Fig. 3(a), its large ST current $i_{\rm ST}$ is then supplied mostly through N_3 with L_{K3} in series, since the current through C_2 has been limited by $L_{\rm in}$ to the filtered input current $I_{\rm in}$. Respective winding currents through N_1, N_2, and N_3 in the state can also be determined as

$$i_1 = 0 \tag{1}$$

$$i_3 = -i_2 = K\frac{P}{V_{\rm in}} \tag{2}$$

where $K = \frac{N_1+N_3}{N_3-N_2}$, and P is the power.

Subsequently, at the instant of crossover to the NST state in Fig. 3(b), L_{K3} and C_2 must instantaneously change to supply the predetermined inductive load current I_o. Unfortunately, both L_{K3} and C_2 do not permit instantaneous changes, since current through C_2 comes from $L_{\rm in}$ and L_{K1}. A mismatch thus occurs, which will abnormally force the currents through L_{K1} and L_{K3} (L_{K2} too according to circuit laws) to change abruptly during the ST to NST crossover. These give rise to high voltage spikes throughout the I-YSI, including at its dc-link. Eventually, the winding currents stabilize to values expressed below in the NST state

$$i_1 = \frac{P}{(1-d)V_{\rm in}} \tag{3}$$

$$i_2 = \frac{KdP}{(1-d)V_{\rm in}} \tag{4}$$

$$i_3 = \frac{(1-Kd)P}{(1-d)V_{\rm in}} \tag{5}$$

where d is the ST duty ratio.

Clearly, a method to solve the problem is to provide an alternative capacitive path across the dc-link only during the ST to NST crossover. This method has smoothly been realized by the proposed HS-YSI, as demonstrated in subsequent sections.

III. High-Step-Up Y-Source Inverter

Fig. 4 shows the proposed HS-YSI with its absorbing circuit comprising C_3, C_4, D_2, and L_o (in red). Like all impedance-source inverters, it has two board operational modes, notated as ST and NST, respectively. But, due to leakage influences from its coupled inductor and the nonideal of semiconductor devices, these two operational modes can be further divided, as explained below.

A. Operational Modes

Fig. 5 shows operational modes of the HS-YSI, where the inverter bridge and ac load have been simplified as a switch *SW* and a current source I_o in parallel. Response times of the switches and diodes have also been assumed to be much shorter than consequential inductive and/or capacitive transitional times. This is especially true, if C_1, C_2, C_3, and C_4, and L_{in}, L_o, and L_M are chosen large enough, so that their respective voltages and currents are almost constant during one switching period. It should however be noted that, unlike the others, L_M does not represent a discrete inductor. Rather, it represents the equivalent magnetizing inductance of the three-winding coupled inductor, which in practice, also has a small leakage inductance in series with each winding. There are therefore three small leakage inductances, drawn with red wavy lines in Fig. 5, whose currents are not constant over a switching period. Key waveforms for illustrating them are summarized in Fig. 6, where each switching period has been divided into six intervals to be described next.

1) ST States: $[t_0, t_1]$: Switch *SW* begins to turn ON at t_0, but because of leakage inductance of winding N_1, diode D_1 continues to conduct, while diode D_2 remains reverse-biased. Voltage across *SW*, which is also the dc-link voltage, then begins to drop. This causes voltages across the three leakage inductances to change. Moreover, by tracing through the circuit, it has been found that components of current flowing through *SW* are all limited by inductances. The turning ON of *SW* is therefore realized with zero current at t_0, over this very short semiconductor-switching subinterval.

$[t_1, t_2]$: Voltage across *SW* drops to zero, while its current increases significantly. Windings N_2 and N_3 are now clamped by voltages of C_1 and C_4 in series, while N_1 and N_3 are clamped by C_2, since D_1 is still conducting. Current through D_1 is, in fact, falling at a rate mostly determined by its parasitic capacitance resonating with leakage inductance of N_1.

$[t_2, t_3]$: The final ST state has been entered with both D_1 and D_2 reverse-biased. It is the longest among the three ST subintervals, during which, L_{in}, L_o, and L_M charge linearly, while C_1 to C_4 discharge linearly.

2) NST States: $[t_3, t_4]$: Switch *SW* turns OFF at t_3, causing its voltage and current to rise and fall, respectively, over this very short semiconductor-switching subinterval. Simultaneously, reverse voltages and forward currents of D_1 and D_2 begin to drop and rise. At the end of the subinterval, the dc-link voltage across *SW* becomes slightly higher than its final NST value, but still significantly smaller than voltage spikes caused by leakage inductances, if an absorbing circuit has not been added.

$[t_4, t_5]$: Diodes D_1 and D_2 start to conduct. The three leakage inductances can then form resonating meshes with capacitances in the circuit. In total, three meshes can be drawn with windings of the coupled inductor included. They are mesh 1 formed by N_2, N_3, C_1, and C_3, mesh 2 formed by N_1, N_3, and C_2, and mesh 3 formed by N_1, N_2, C_1, L_{in}, and the input dc source. During this subinterval, the conduction of D_2 also permits C_3 and C_4 to be connected in series for clamping the dc-link voltage across *SW*. Voltage spikes have hence been intentionally suppressed at ST to NST crossovers.

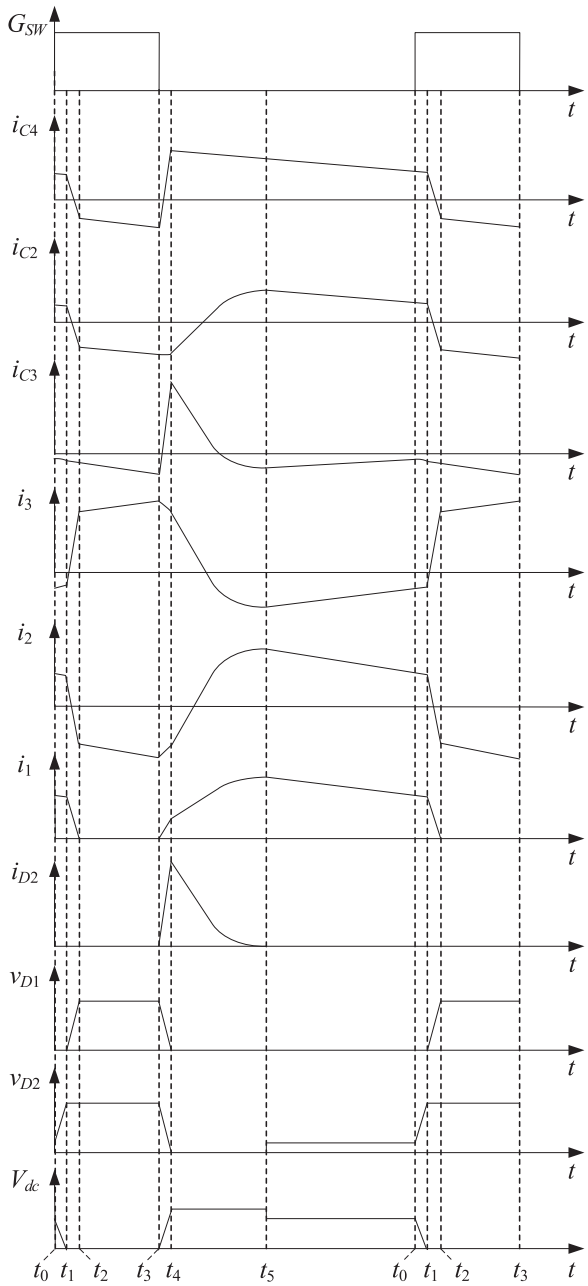

Fig. 6. Key waveforms of HS-YSI with respect to equivalent circuits in Fig. 4.

$[t_5, t_0]$: This is the final NST state entered, after current of D_2 drops to zero and it begins to block. Meanwhile, D_1 continues to conduct, which hence permits C_2 to be connected across N_1 and N_3 for clamping their total voltage. Additionally, the dc-link voltage across *SW* is no longer solely equal to the combined voltage of C_3 and C_4 in series, since it now includes the reverse voltage of D_2. There will hence be a very small dc-link voltage drop (proven later), after entering this subinterval at t_5.

B. Current Analysis

To avoid complex current expressions that may not have any analytical value, the equivalent circuits in Fig. 5 have been

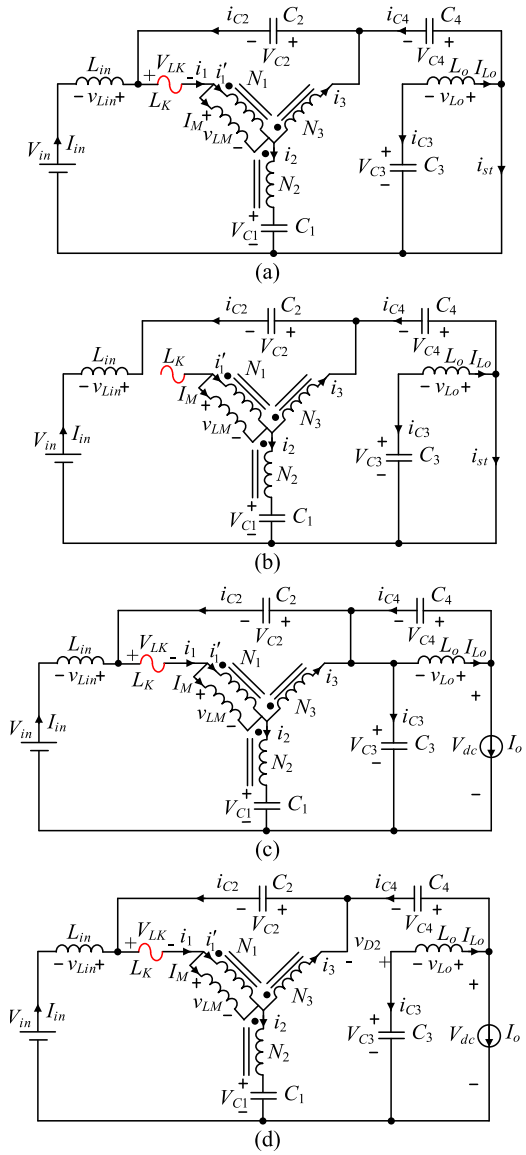

Fig. 7. Simplified equivalent circuits of HS-YSI when in (a) ST state $[t_0, t_2]$, (b) ST state $[t_2, t_4]$, (c) NST state $[t_4, t_5]$, and (d) NST state $[t_5, t_0]$.

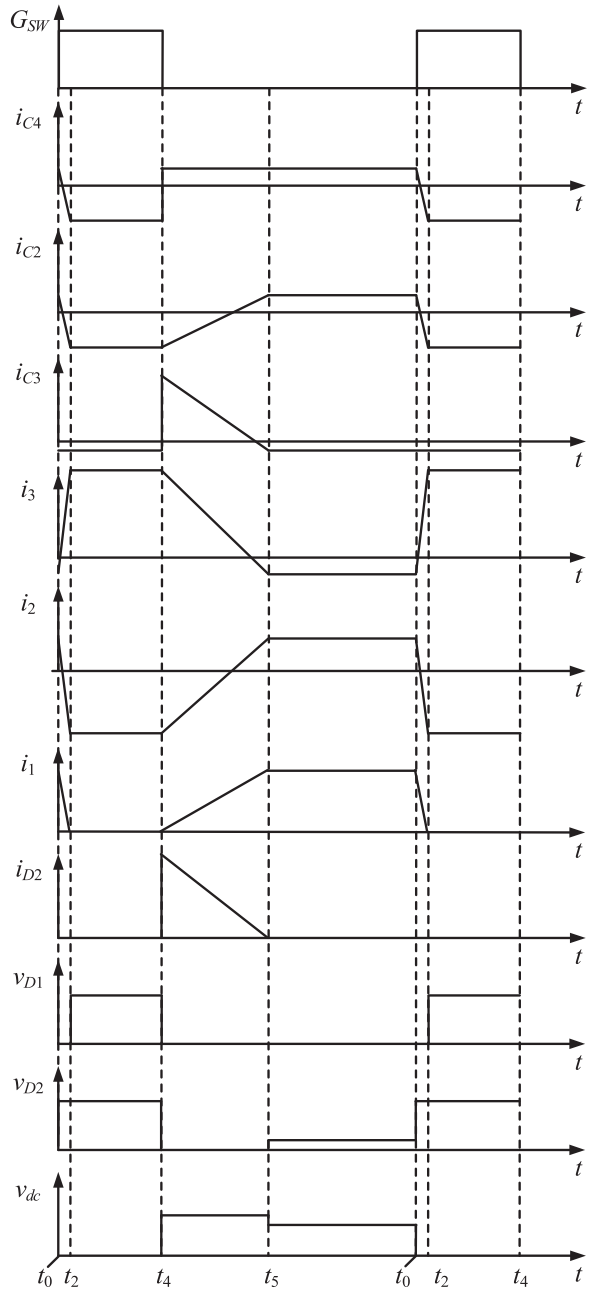

Fig. 8. Simplified key waveforms of HS-YSI with respect to equivalent circuits in Fig. 7.

simplified to those in Fig. 7, where all leakage inductances have been reflected and summed as L_K in series with N_1. Additionally, since Fig. 5(a) and (d) for representing very short semiconductor-switching subintervals are similar to Fig. 5(f) and (c), they can be ignored, and hence not included in Fig. 7. Fig. 8 then shows simplified key waveforms with only four distinct subintervals and winding currents i_1, i_2, and i_3 assumed to change linearly during $[t_4, t_5]$. This figure, like Fig. 6, again shows that the state in Fig. 7(a) is much shorter in duration than the other three states. It is nonetheless included for showing influences caused by leakage inductances. Its circuit expressions have however been omitted from the mathematical analysis, since energies of passive components have hardly changed during such short interval between $[t_0, t_2]$.

Therefore, beginning with Fig. 7(b), where both D_1 and D_2 are blocking, and *SW* is conducting from t_2 to t_4, their related current expressions can be obtained as

$$i_{C1} = i_2 = -i_3 \tag{6}$$

$$i_{C2} = -I_{\text{in}} \tag{7}$$

$$i_{C3} = -I_{Lo} \tag{8}$$

$$i_{C4} = -(I_{\text{in}} + i_3) \tag{9}$$

$$N_1 i_1' + (N_3 - N_2) i_3 = 0 \tag{10}$$

$$i_1' = -I_M \tag{11}$$

where (10) and (11) are for relating currents within the coupled inductor. Substituting them into (6) and (9) then yields the

following current expressions for C_1 and C_4

$$i_{C1} = -\frac{N_1}{N_3 - N_2} I_M \tag{12}$$

$$i_{C4} = -I_{\text{in}} - \frac{N_1}{N_3 - N_2} I_M . \tag{13}$$

The capacitor currents will change, after progressing to Fig. 7(c), where both D_1 and D_2 are conducting, while *SW* is blocking from t_4 to t_5. Collectively, they cause currents i_2 and i_{C2} to increase linearly without any abrupt step at t_4. In contrast, i_{C4} and i_{C3} change abruptly at t_4 to

$$i_{C4} = I_{Lo} - I_o \tag{14}$$

$$i_{C3} = I_{\text{in}} - I_o + \frac{N_1}{N_3 - N_2} I_M . \tag{15}$$

These capacitor currents will again change, after entering the state in Fig. 7(d), where D_2 has stopped conduction, and hence leads to the following new set of current expressions:

$$i_{C3} = -I_{Lo} \tag{16}$$

$$i_{C4} = I_{Lo} - I_o \tag{17}$$

$$i_{C1} = i_2 \tag{18}$$

$$i_1 = I_{\text{in}} + i_{C2} \tag{19}$$

$$i_3 = I_o - I_{Lo} + i_{C2} \tag{20}$$

$$i_2 = I_{\text{in}} + I_{Lo} - I_o \tag{21}$$

$$N_1 i_1' + N_2 i_2 + N_3 i_3 = 0 \tag{22}$$

$$i_1 = i_1' + I_M \tag{23}$$

where (22) and (23) are for the coupled inductor. These new expressions then yield the following currents through C_1 and C_2

$$i_{C1} = I_{\text{in}} + I_{Lo} - I_o \tag{24}$$

$$i_{C2} = \frac{(N_3 - N_2)(I_{\text{in}} + I_{Lo} - I_o) + N_1 I_M}{N_3 + N_1} - I_{\text{in}} . \tag{25}$$

Related current expressions for each capacitor can now be current-second integrated over a switching period, as expressed below

$$\begin{aligned} &\int_{t_2}^{t_4} i_{Cx} dt + \int_{t_4}^{t_5} i_{Cx} dt + \int_{t_5}^{t_0} i_{Cx} dt \\ &= \int_0^{dT} i_{Cx} dt + \int_{dT}^{(\alpha+d)T} i_{Cx} dt + \int_{(\alpha+d)T}^{T} i_{Cx} dt \\ &= 0 \end{aligned} \tag{26}$$

where $\alpha = \frac{t_5 - t_4}{T}$ is the proportionality coefficient, $x = 1, 2, 3$ or 4 is an index for the capacitors, and interval $[t_0, t_2] \approx 0$ has been omitted.

Eventually, the following current expressions can be derived, from which currents through all components of the impedance network can be computed

$$\alpha = \frac{2}{1 + K}(1 - d) \tag{27}$$

$$I_{Lo} = I_{\text{in}} \tag{28}$$

$$I_M = \frac{(N_1 + N_3)}{N_1} I_{\text{in}} \tag{29}$$

$$I_o = \frac{1 - (2 + K)d}{(1 - d)} I_{\text{in}} . \tag{30}$$

C. Voltage Analysis

In terms of voltages, equivalent circuits in Fig. 7(a) and (b) can be analyzed as a single ST state with *SW* conducting from t_0 to t_4. The conduction of *SW*, in turn, causes C_1 and C_4 to be connected in series for clamping N_2 and N_3 of the coupled inductor. Relevant voltage expressions can thus be written as

$$v_{LM} = (V_{C1} + V_{C4}) \frac{N_1}{N_3 - N_2} \tag{31}$$

$$v_{Lo} = -V_{C3} \tag{32}$$

$$v_{L\text{in}} = -(V_{\text{in}} + V_{C2} + V_{C4}) \tag{33}$$

where V_{C1}, V_{C2}, V_{C3}, and V_{C4} are voltages across C_1, C_2, C_3, and C_4, and v_{LM}, v_{Lo}, and $v_{L\text{in}}$ are voltages across L_M, L_o, and L_{in}, respectively.

Upon turning OFF *SW*, the first NST state entered is shown in Fig. 7(c), where leakage current through L_K starts to increase linearly from t_4 to t_5. During this time, N_2 and N_3 are also clamped by C_1 and C_3 in series, which together with other circuit features, permit voltages across various inductances to be derived as

$$v_{LM} = (V_{C1} - V_{C3}) \frac{N_1}{N_3 - N_2} \tag{34}$$

$$v_{Lo} = V_{C4} \tag{35}$$

$$v_{L\text{in}} = V_{C3} - V_{C2} - V_{\text{in}} \tag{36}$$

$$v_{LK} = -(V_{C1} - V_{C3}) \frac{N_1 + N_3}{N_3 - N_2} - V_{C2} . \tag{37}$$

Moreover, since leakage current through L_K increases linearly from zero at t_4, its current $i_1(t_5)$ at t_5 can promptly be expressed as

$$i_1(t_5) = 0 + \frac{1}{L_K} \int_{dT}^{(d+\alpha)T} v_{LK} dt \tag{38}$$

which together with (20), (25), (27), (28), (29), and (30), permits voltage across L_K to be derived as

$$v_{LK} = \frac{(1 + K)^2}{2(1 - d)^2 KT} I_{\text{in}} L_K . \tag{39}$$

The NST state then changes to Fig. 7(d), in which N_1, N_3, and L_K are clamped by C_2 during $[t_5, t_0]$. Leakage L_K and magnetizing L_M will hence share V_{C2} proportionally. These observations permit voltages across various inductances to be

expressed as

$$v_{LM} = (V_{C1} - V_{C3} + v_{D2})\frac{N_1}{N_3 - N_2} \tag{40}$$

$$v_{Lo} = V_{C4} - v_{D2} \tag{41}$$

$$v_{Lin} = V_{C3} - V_{C2} - V_{in} - v_{D2} \tag{42}$$

$$v_{LK} = -V_{C2}\frac{L_K}{L_K + (1 + \frac{N_3}{N_1})L_M}$$

$$= -(V_{C1} - V_{C3} + v_{D2})\frac{N_1 + N_3}{N_3 - N_2} - V_{C2}. \tag{43}$$

Moreover, since $L_K \ll L_M$, v_{LK} in (43) can be approximated as zero from t_5 to t_0, and by substituting (37) and (39) into it, voltage across the reverse-biased D_2 can be derived as

$$v_{D2} = \frac{(1+K)^2}{2(1-d)^2K^2T} I_{in} L_K. \tag{44}$$

Later, by substituting numerical values to it, v_{D2} can be proven to be very small, and can hence be safely omitted during $[t_5, t_0]$ to simplify the final derived expressions that causes the voltages across various inductances in Fig. 7(c) and (d) to be the same, which can then be applied to derive the following voltage relationship:

$$(V_{C3} - V_{C1})\frac{N_1 + N_3}{N_3 - N_2} - V_{C2} = v_{D2}\frac{N_1 + N_3}{N_3 - N_2} \approx 0. \tag{45}$$

All derived voltage expressions for each inductor can follow-up to be volt-second integrated over a switching period T, in accordance to

$$\int_{t_0}^{t_4} v_{Lx}dt + \int_{t_4}^{t_0} v_{Lx}dt = \int_0^{dT} v_{Lx}dt + \int_{dT}^{T} v_{Lx}dt = 0 \tag{46}$$

where L_x represents L_M, L_o or L_{in}. Performing the integration finally leads to the following voltages across C_1, C_2, C_3, and C_4

$$V_{C1} = (1-2d)BV_{in} \tag{47}$$

$$V_{C2} = dKBV_{in} \tag{48}$$

$$V_{C3} = (1-d)BV_{in} \tag{49}$$

$$V_{C4} = dBV_{in} \tag{50}$$

where $B = \frac{1}{1-(2+K)d}$ is the voltage gain, and K is the turns ratio of the coupled inductor. A gain higher than that of the original Z-source inverter can thus be obtained by setting K equal or greater than one.

Regardless of that, the dc-link voltage V_{dc} and peak ac output voltage $\hat{v}_o$ of the inverter are always expressed as

$$V_{dc} = BV_{in} \tag{51}$$

$$\hat{v}_o = BMV_{in} \tag{52}$$

where M is the modulation index, which together with d, must satisfy

$$M < 1 - d \tag{53}$$

$$1 - (2+K)d > 0. \tag{54}$$

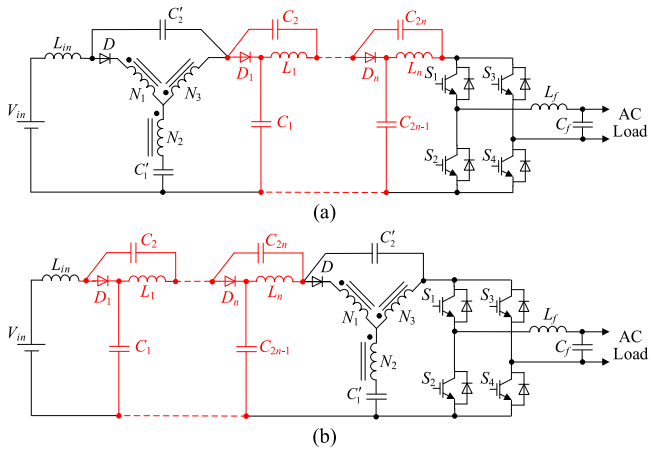

Fig. 9. HS-YSIs with multiple cascaded absorbing circuits.

TABLE I
VOLTAGE GAINS OF DIFFERENT IMPEDANCE-SOURCE INVERTERS WITH COUPLED INDUCTORS

Impedance Network	Gain B=V_{dc}/V_{in}	Turns ratio K
T- or Trans-Z-source [12][20]	1/(1-Kd)	(N_1+N_2)/N_2
Γ-Z-Source [15]	1/(1-Kd)	N_2/(N_2-N_1)
Y-Source [17]	1/(1-Kd)	(N_1+N_3)/(N_3-N_2)
LCCT-Z-Source [14]	1/[1-(1+K)d]	N_1/N_2
Improved-Trans-Z-source [21]	1/[1-(1+K)d]	(N_1+N_2)/N_2
Improved-Y-source [18]	1/[1-(1+K)d]	(N_1+N_3)/(N_3-N_2)
HS-YSI (n = 1)	1/[1-(1+n+K)d]	(N_1+N_3)/(N_3-N_2)

A larger d to obtain a bigger gain will hence limit the maximum of M, together with some deterioration of output waveform quality. One method to lower d and raise M without compromising gain is to introduce a larger K. Alternatively, multiple cascaded absorbing circuits can be introduced. Fig. 9 shows two possible topologies, whose cascaded absorbing circuits (in red) are placed at different locations. Despite that, they can both eliminate dc-link voltage spikes at instants of ST to NST crossovers. In Fig. 9(a), it is ensured by the conduction of D_n, which in turn, causes C_{2n-1} and C_{2n} to be in series across the dc-link of the inverter bridge. The same conduction of D_n in Fig. 9(b) also permits C_2', C_{2n}, and C_{2n-1} to clamp the dc-link voltage. Both inverters in Fig. 9 are therefore effective, and have a common gain, expressed as

$$B = \frac{1}{1-(1+n+K)d} \tag{55}$$

where n is the number of absorbing circuits cascaded together, which unquestionably, is an additional parameter for tuning the gain of the inverter.

The main disadvantage here is more discrete components, which in practice, should be avoided, if varying K of the coupled inductor can produce the same effect. Thus, the number of cascaded absorbing circuits should be limited. Nonetheless, the gain in (55) is summarized in Table I for comparison with those of the existing impedance-source inverters. In case of HS-YSI, n equals one, which still gives a higher gain than existing impedance-source inverters, if they use the same K and d. The

TABLE II
VOLTAGE GAINS OF HS-YSI UNDER DIFFERENT WINDING FACTOR AND TURNS RATIO

K	d_{max}	Voltage gain B	N_1:N_2:N_3
2	1/4	$(1\text{-}4d)^{-1}$	(1:1:3), (2:1:4), (1:2:5)
3	1/5	$(1\text{-}5d)^{-1}$	(1:1:2), (3:1:3), (4:2:5)
4	1/6	$(1\text{-}6d)^{-1}$	(2:1:2), (1:2:3), (5:1:3)
5	1/7	$(1\text{-}7d)^{-1}$	(3:1:2), (2:2:3), (1:3:4)
6	1/8	$(1\text{-}8d)^{-1}$	(4:1:2), (3:2:3), (2:3:4)
7	1/9	$(1\text{-}9d)^{-1}$	(5:1:2), (4:2:3), (3:3:4)

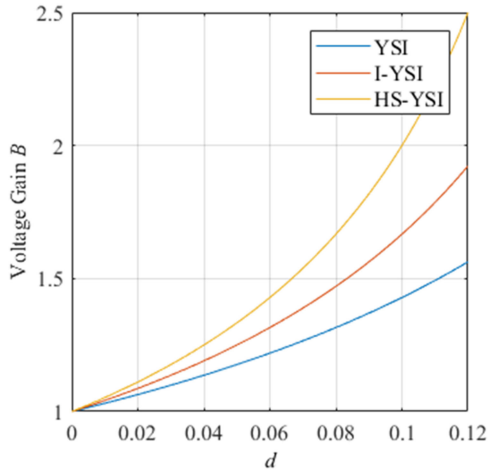

Fig. 10. Voltage gains of different YSIs versus duty cycle.

same K can, in turn, be realized with different $N_1 : N_2 : N_3$ ratios for a three-winding coupled inductor, as seen from Table II. Voltage gains of a few inverters in Table I, namely, the YSI, I-YSI, and HS-YSI, can subsequently be plotted in Fig. 10, where it can be seen that if the three inverters have the same duty cycle, output voltage of the HS-YSI is higher than those of the YSI and I-YSI.

D. Stresses and Lifetime

From earlier derivations, expressions for calculating voltage and current stresses experienced by components of the HS-YSI can be extracted and summarized in Table III. Also added to the table are corresponding expressions for the I-YSI in Fig. 1. Both inverters can then be compared under various conditions. For instance, if they have the same gain B and duty ratio d, their respective turns ratios must satisfy $K_c = 1 + K$, where subscript c has been added for representing the I-YSI. More turns are thus needed by the I-YSI, whose voltage stresses across C_1, C_2, and D_1 are also higher than those of the HS-YSI. The HS-YSI however experiences a high voltage stress across D_2, which must hence be sized appropriately.

As for their coupled inductors, maximum currents flowing through N_1 and N_2 of the HS-YSI are larger than those of the I-YSI, while its current through N_3 may either be less than or equal to that of the I-YSI, depending on the values of K and d. Despite that, ST current stresses experienced by the switches of the inverter bridges are quite close for both inverters, according to entries for i_{ST} in Table III.

TABLE III
COMPARISON OF VOLTAGE AND CURRENT STRESSES FOR TWO INVERTERS

Parameter for Comparison	I-YSI	HS-YSI
$B=V_{dc}/V_{in}$	$1/[1\text{-}(1+K_c)d]$	$1/[1\text{-}(2+K)d]$
V_{C1}	$(1\text{-}d)BV_{in}$	$(1\text{-}2d)BV_{in}$
V_{C2}	dK_cBV_{in}	$dKBV_{in}$
V_{C3}	NA	$(1\text{-}d)BV_{in}$
V_{C4}	NA	dBV_{in}
V_{D1}	K_cBV_{in}	KBV_{in}
V_{D2}	NA	BV_{in}
I_{in}	P/V_{in}	P/V_{in}
I_{Lo}	NA	P/V_{in}
i_1	$P/(1\text{-}d)V_{in}$	$(1+K)P/(1\text{-}d)KV_{in}$
i_2	K_cP/V_{in}	$(1+K)P/(1\text{-}d)V_{in}$
i_3	K_cP/V_{in}	KP/V_{in} or $(K^2\text{-}1)P/(1\text{-}d)KV_{in}$
i_{ST}	$(1+K_c)P/V_{in}$	$(2+K)P/V_{in}$

As for their lifetimes, a simple comparison may be provided, based on the understanding that lifetime of a system is mainly determined by the component with the shortest lifetime. This component is likely a capacitor in the HS-YSI, since the lifetime of its added diode is always several times higher. Therefore, only the lifetime of the deciding capacitor is assessed, which from [25], may be computed using

$$\mathrm{LT} = \mathrm{LT}_0 \times \left(\frac{V}{V_0}\right)^{-n} \times 2^{\frac{T_0 - T}{10}} \tag{56}$$

where n is an exponential index, and LT and LT_0 are lifetimes under normal usage and testing conditions, respectively. For both conditions, V and V_0 represent voltages across the capacitor, and T and T_0 represent their temperatures in Kelvin.

By next comparing expressions in Table III, it can be determined that for the I-YSI and HS-YSI, their ST ratios must satisfy $d < d_c$, if their parameters are set as $K = K_c$ and $B = B_i$, where subscript c has been added for notating the I-YSI. This then leads to capacitor C_3 in the HS-YSI shouldering a higher voltage stress and a shorter lifetime according to (56).

The outcome will however change, if parameters of the two inverters are alternatively set to $d = d_c$ and $B = B_c$. Their winding factors must then satisfy $K = K_c - 1$, or in other words, winding factor of the HS-YSI is smaller than that of the I-YSI to attain the same performance. That setting causes capacitor C_1 in the I-YSI and capacitor C_3 in the HS-YSI to have similarly high voltage stresses. Their lifetimes are therefore comparable. Besides, because the higher voltage stress in the poststage, the HS-YSIs with multiple cascaded absorbing circuits have shorter lifetimes.

IV. EXTRA POWER LOSSES

Additional components found in the HS-YSI will undeniably introduce extra losses. It may thus be necessary to quantify these losses, which are mostly contributed by diode D_2 and inductor L_o (losses from capacitors C_3 and C_4 are comparably less significant). Expressions for computing these losses are hence derived, as presented below.

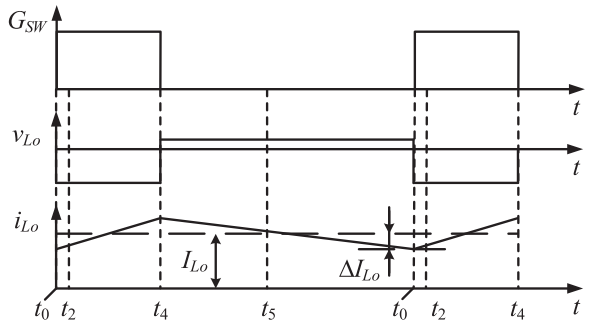

Fig. 11. Key waveforms of inductor L_o.

A. Losses From L_o

Fig. 11 shows key waveforms of L_o, whose losses include hysteresis loss P_H and copper loss P_{Cu}. The latter can be calculated using

$$P_{\mathrm{Cu}} = i_{Lo-\mathrm{rms}}^2 R \tag{57}$$

where *R* is the winding resistance and $i_{Lo-\mathrm{rms}}$ is the root-mean-square current through L_o.

Further, since current ripple ΔI_{Lo} of L_o is relatively small, it can be ignored, resulting in $i_{Lo-\mathrm{rms}} = I_{Lo}$, where I_{Lo} is the dc component of i_{Lo}. Therefore, (57) can be rewritten as

$$P_{\mathrm{Cu}} = I_{Lo}^2 R. \tag{58}$$

On the other hand, P_H is caused by the ac component of i_{Lo}, which in theory, can be determined using

$$P_H = a_1 B_{pk}^{b_1} f^{c_1} \tag{59}$$

where a_1, b_1, and c_1 are constants determined by curve-fitting of the recorded core losses [26], and *f* is the applied frequency. The flux density B_{pk} may then be calculated from

$$B_{pk} = \frac{\Delta B}{2} = \frac{B_{\mathrm{AC-max}} - B_{\mathrm{AC-min}}}{2} \tag{60}$$

where ΔB is the AC flux swing between maximum $B_{\mathrm{AC-max}}$ and minimum $B_{\mathrm{AC-min}}$.

Since the flux density can further be expressed in terms of magnetizing field *H*, related maximum and minimum of *H* can preliminarily be obtained from

$$H_{\mathrm{AC-max}} = \frac{N}{l_e}\left(I_{Lo} + \Delta I_{Lo}\right) \tag{61}$$

$$H_{\mathrm{AC-min}} = \frac{N}{l_e}\left(I_{Lo} - \Delta I_{Lo}\right). \tag{62}$$

From (61) and (62), $B_{\mathrm{AC-max}}$ and $B_{\mathrm{AC-min}}$ can eventually be expressed as

$$B_{\mathrm{AC-max}} = \left[\frac{a_2 + b_2 H_{\mathrm{AC-max}} + c_2 H_{\mathrm{AC-max}}^2}{1 + d_2 H_{\mathrm{AC-max}} + e_2 H_{\mathrm{AC-max}}^2}\right]^x \tag{63}$$

$$B_{\mathrm{AC-min}} = \left[\frac{a_2 + b_2 H_{\mathrm{AC-min}} + c_2 H_{\mathrm{AC-min}}^2}{1 + d_2 H_{\mathrm{AC-min}} + e_2 H_{\mathrm{AC-min}}^2}\right]^x \tag{64}$$

where a_2, b_2, c_2, d_2, e_2, and x are magnetization constants determined from appropriate curve-fitting [26].

TABLE IV
SYSTEM PARAMETERS

Parameter	Value/Part Number
Input voltage	80 V
Load resistance	60 Ω (200 W)
Capacitances C_1 and C_3	470 μF
Capacitances C_2 and C_4	100 μF
Inductances L_{in} and L_o	4.3 mH
Switching frequency f_{sw}	10 kHz
Turns ratio N_1:N_2:N_3	40:40:80
Core	C055863A2
Switches	IRGP4062DPbF
Diodes D_1 and D_2	30EPH06PBF
Filter inductance L_f	5.6 mH
Filter capacitance C_f	4.7 μF

B. Losses From D_2

Losses from D_2 include conduction loss P_f, reverse recovery loss P_r, and reverse leakage loss P_l. However, from Fig. 8, it can be seen that current through D_2 slowly drops to zero at t_5, which in other words, means P_r is zero.

In contrast, P_l is not zero, and can be computed using

$$P_l = I_R V_{D2} d \tag{65}$$

where I_R is the reverse current taken from [27].

Conduction loss P_f can also be calculated using

$$P_f = \frac{1}{T}\int_{dT}^{\alpha T + dT} i_{D2} V_F dt \tag{66}$$

where V_F is the forward voltage drop across D_2, whose value can be obtained from [27].

C. Total Extra Loss From HS-YSI

With a nominal output power of 200 W, the total extra loss contributed by additional components L_o and D_2 of the HS-YSI is

$$P_{\mathrm{total}} = P_{\mathrm{Cu}} + P_H + P_l + P_f \approx 5.62\ \mathrm{W}. \tag{67}$$

This extra loss cannot be avoided, but by recycling energy from the leakage inductances, energy wasted in switches can be lowered considerably. Moreover, since voltage spikes are fully eliminated at the dc-link, a lower voltage-rated switch with a lower on-resistance can be chosen for lowering the overall power loss.

V. SIMULATION AND EXPERIMENTAL RESULTS

Simulations and experiments have been performed with the I-YSI in Fig. 1 and HS-YSI in Fig. 4 using the same parameters listed in Table IV. To boost an input voltage of 80 V to an output voltage of 160 V, ST duty ratios of the I-YSI and HS-YSI have been set 0.15 and 0.12, respectively, since they use the same parameters from Table IV and same modulation index of $M = 0.8$. Their respective theoretical voltages can then be determined as $V_{C1} = 170$ V and $V_{C2} = 90$ V for the I-YSI, and $V_{C1} = 152$ V, $V_{C2} = 72$ V, $V_{C3} = 176$ V and $V_{C4} = 24$ V for the HS-YSI. Their dc-link voltages are however the same at

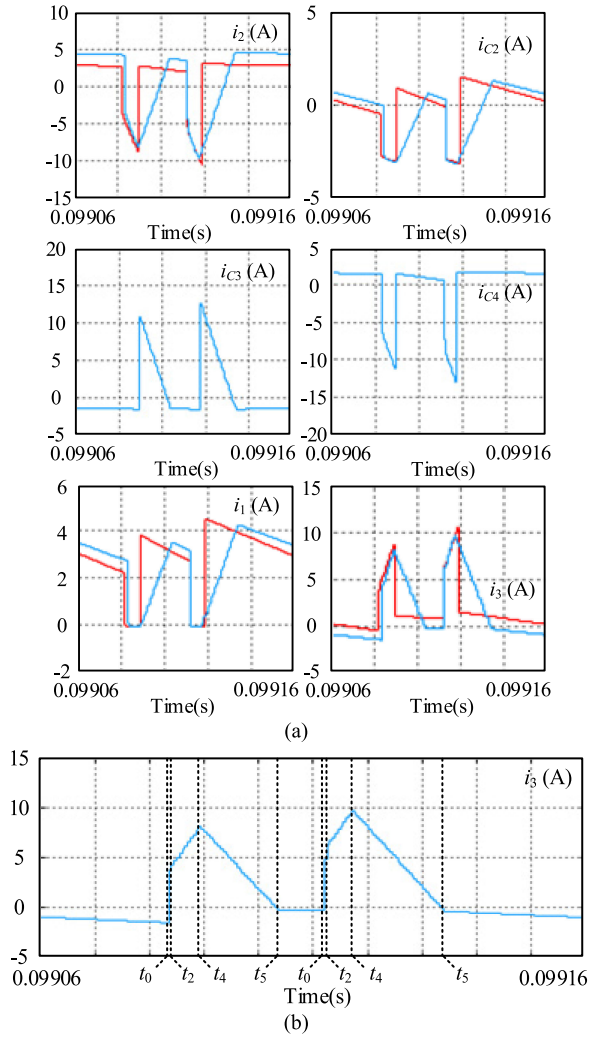

Fig. 12. Simulated. (a) i_2, i_{C2}, i_{C3}, i_{C4}, i_1, i_3. (b) i_3 of I-YSI (red) and HS-YSI (blue).

$V_{\rm dc} = 200$ V. Their respectively obtained results are described next.

A. Simulation Results

The key current waveforms of the two inverters shown in Fig. 12 have been found to match well with theoretical waveforms drawn in Fig. 8. Most importantly, they have demonstrated that all winding current changes through leakage inductances of the HS-YSI have occurred gradually from t_4 to t_5, rather than instantaneously at t_4, after each ST to NST crossover. Voltage spikes are hence not generated by the proposed HS-YSI.

B. Experimental Results

A 200-W prototype controlled by a TMS320F2812 digital signal processor has been built and shown in Fig. 13. It can be configured as either the I-YSI in Fig. 1 or HS-YSI in Fig. 4, using the same parameters provided in Table IV. Its coupled inductor has also been loosely wound to better demonstrate the effects from leakage inductances, as seen from Fig. 14, where

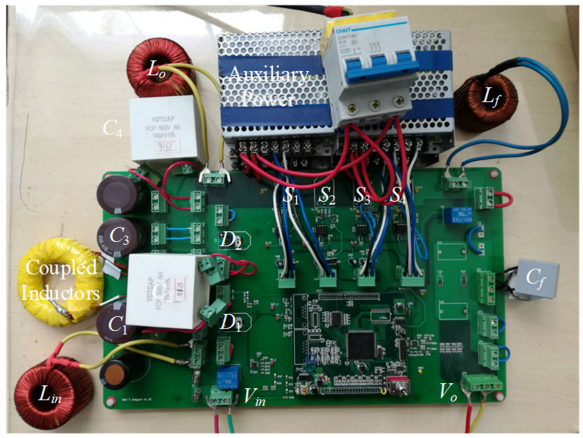

Fig. 13. Laboratory setup of a 200-W inverter.

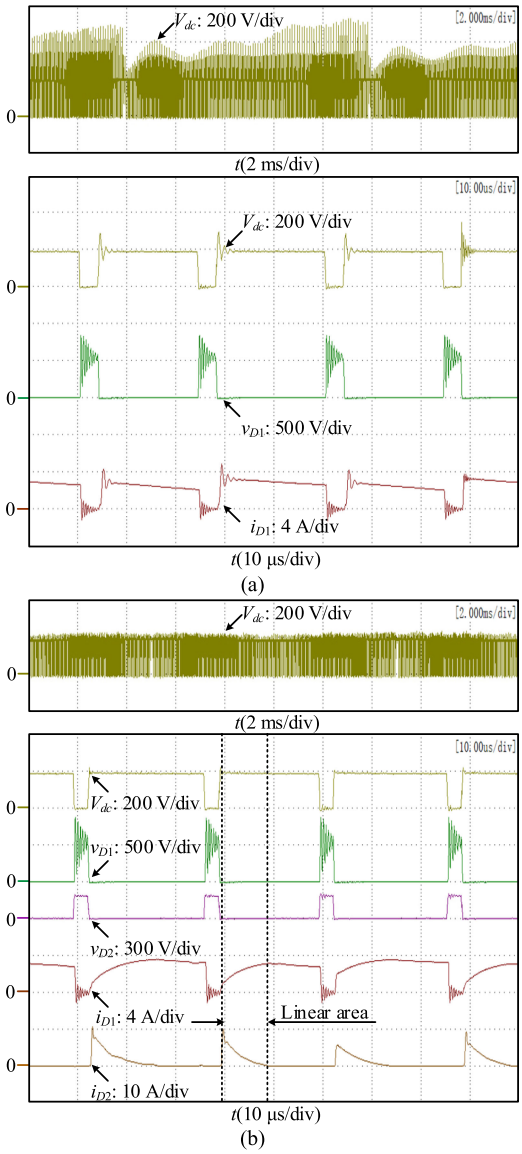

Fig. 14. Measured results of $V_{\rm dc}$, v_{D1}, v_{D2}, i_{D1}, and i_{D2}. (a) I-YSI. (b) HS-YSI at 200 W operation.

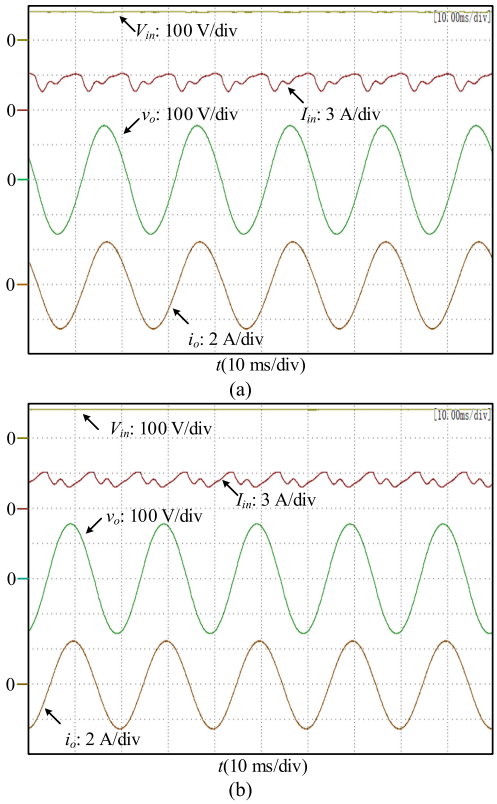

Fig. 15. Measured input voltages V_{in}, input currents I_{in}, output voltages v_o, and output currents i_o. (a) I-YSI. (b) HS-YSI at 200 W operation.

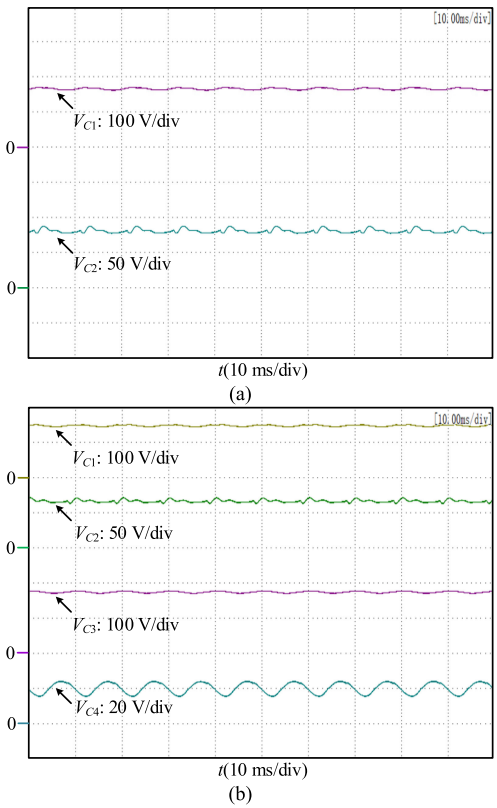

Fig. 16. Measured capacitors voltages. (a) I-YSI. (b) HS-YSI.

dc-link voltages, voltages and currents of diodes are plotted. Clearly, the dc-link voltage spikes of the I-YSI can reach 530 V, even though its stabilized value is only 194 V. It is thus inferior, as compared to the HS-YSI, whose dc-link voltage of 195 V is nearly free of spikes.

Other key features from waveforms of the HS-YSI in Fig. 14(b) have also been found to match well with those from the theoretical waveforms drawn in Fig. 5. For example, the time duration from t_4 to t_5 in Fig. 14(b) has been measured as 0.438 T, while that in Fig. 8 or from (27) is 0.44 T, where T is the switching period. Furthermore, from (44) and using parameters from Table IV, v_{D2} has been determined as $2.87 \times 10^4 L_K$ from t_5 to t_0. Its value is thus only a few mV, since the leakage L_K is usually from 10 nH to 10 μH. It is thus expected to be unnoticeable, as verified by the third trace in Fig. 14(b).

Corresponding dc input and ac output waveforms are then shown in Fig. 15, where double-line-frequency ripples can noticeably be seen from input currents of both inverters [28], [29]. The ripples are however slightly smaller in the HS-YSI, where more passive components are used for filtering. Their peak ac output voltages have also been read as 155 V for both the I-YSI and the HS-YSI. Both values are smaller than their common theoretical value of 160 V, because of reduction of effective ST duty ratio caused by leakage inductances and ESRs [24]. Other than these, most theoretical and experimental values have been found to match closely, like $V_{C1} = 169$ V and $V_{C2} = 86$ V measured in Fig. 16(a) for the I-YSI, and $V_{C1} = 150$ V, $V_{C2} = 69$ V, $V_{C3} = 176$ V and $V_{C4} = 20$ V from Fig. 16(b) for the HS-YSI.

Follow-up with Fig. 17 shows that the winding currents of the coupled inductor, which for the HS-YSI, change more gradually in the NST state, rather than jump abruptly at the considered ST to NST crossover. However, both I-YSI and HS-YSI exhibit oscillatory currents, which may be due to leakage inductances interacting with parasitic capacitances of the semiconductors. Meanwhile, the HS-YSI operating with a higher gain has been tested by increasing its shoot-though duty ratio d to 0.15 with the other parameters kept unchanged. The new boost ratio B, theoretical dc-link voltage V_{dc}, and output peak voltage computed are thus 4, 320, and 256 V, respectively. Obtained experimental results are given in Fig. 18, where V_{dc} and output peak voltage are 296 and 235 V, respectively. The output voltage loss is thus 256–235 = 21 V due mainly to leakage of the coupled inductor and ESRs in the circuit. Especially with ESRs, their effects increase sharply with gain like most boost converters. They thus cause output voltage loss with $B = 4$ to be greater than that with $B = 2.5$. Despite that, voltage spikes at the dc-link for both cases have been suppressed noticeably, as seen from Figs. 14(b) and 18.

Last but not least, Fig. 19 shows measured efficiencies of the I-YSI and HS-YSI, from which it can be seen that when the power level is low, efficiency of the I-YSI with fewer components is higher than that of the HS-YSI. The reverse is however observed at a higher power level, likely due to leakage energy recovered by the HS-YSI to prevent spikes being higher than losses from the additional components. Another comparison may also be

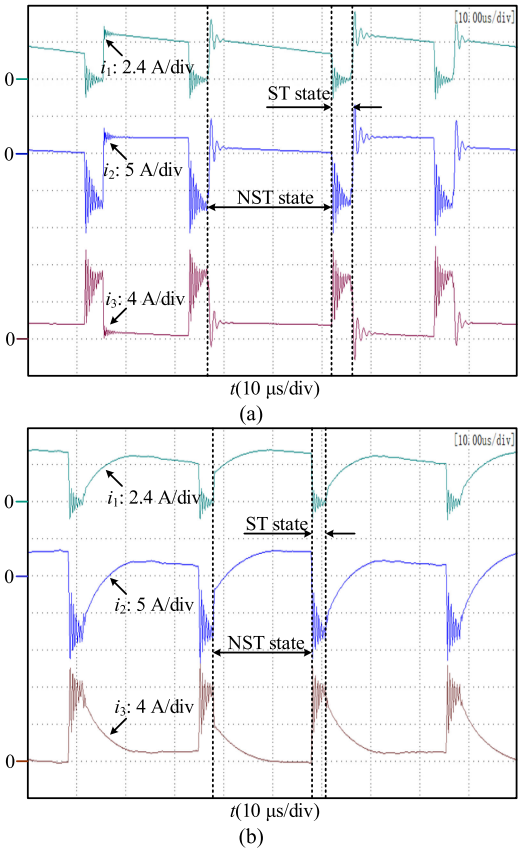

Fig. 17. Measured winding currents i_1, i_2, and i_3. (a) I-YSI. (b) HS-YSI.

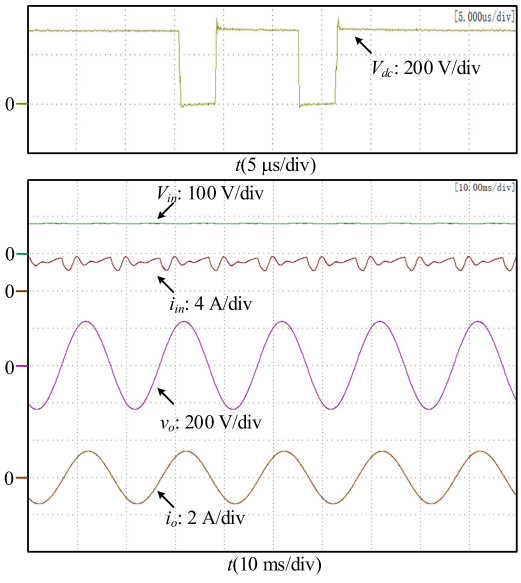

Fig. 18. Measured results of $V_{\rm dc}$, $V_{\rm in}$, V_o, $I_{\rm in}$, and I_o for HS-YSI.

performed by adding the absorbing circuit in Fig. 2(c) to the I-YSI. The obtained effect is an efficiency that is always higher than those of the I-YSI without the absorbing circuit and HS-YSI. However, voltage spikes at dc-link of the I-YSI cannot be sufficiently reduced by the absorbing circuit in Fig. 2(c). Its lifting of gain is also not as prominent as the HS-YSI.

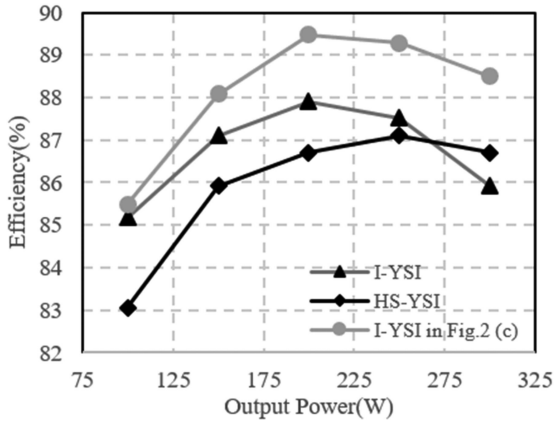

Fig. 19. Efficiency comparison of the I-YSI, I-YSI with absorbing circuit in Fig. 2(c) and HS-YSI.

VI. Conclusion

In this paper, an HS-YSI with a unique absorbing circuit has been proposed for eliminating dc-link voltage spikes without demanding extra switches and compromising the voltage gain. Its gain has, in fact, been improved, when compared with the I-YSI published recently in the literature. The same absorbing circuit can also be used with other impedance-source inverters realized with coupled inductors. It is therefore a universal circuit for removing dc-link voltage spikes, regardless of the number of coupled windings. Simulation and experimental results have verified its effectiveness, when compared with the I-YSI.

References

[1] F. Z. Peng, "Z-source inverter," *IEEE Trans. Ind. Appl.*, vol. 39, no. 2, pp. 504–510, Mar./Apr. 2003.
[2] J. Anderson and F. Z. Peng, "Four quasi-Z-source inverters," in *Proc. Power Electron. Spec. Conf.*, 2008, pp. 2743–2749.
[3] M. Zhu, K. Yu, and F. L. Luo, "Switched inductor Z-source inverter," *IEEE Trans. Power Electron.*, vol. 25, no. 8, pp. 2150–2158, Aug. 2010.
[4] M. -K. Nguyen, Y. -C. Lim, and G. -B. Cho, "Switched-inductor quasi-z-source inverter," *IEEE Trans. Power Electron.*, vol. 26, no. 11, pp. 3183–3191, Aug. 2011.
[5] A. -V. Ho, T. -W. Chun, and H. -G. Kim, "Extended boost active-switched-capacitor/switched-inductor quasi-z-source inverters," *IEEE Trans. Power Electron.*, vol. 30, no. 10, pp. 5681–5690, Oct. 2015.
[6] M. Ismeil, M. Orabi, R. Kennel, O. Ellabban, and H. Abu–Rub, "Experimental studies on a three phase improved switched z-source inverter," in *Proc. Annu. Appl. Power Electron. Conf. Expo.*, 2014, pp. 1248–1254.
[7] A. Chub, O. Husev, J. Zakis, and J. Rabkowski, "Switched-capacitor current-fed quasi-z-source inverter," in *Proc. 14th Biennial Baltic Electron. Conf.*, 2014, pp. 229–232.
[8] C. J. Gajanayake, F. L. Luo, H. B. Gooi, P. L. So, and L. K. Siow, "Extended-boost z-source inverters," *IEEE Trans. Power Electron.*, vol. 25, no. 10, pp. 2642–2652, Oct. 2010.
[9] D. Vinnikov, I. Roasto, T. Jalakas, R. Strzelecki, and M. Adamowicz, "Analytical comparison between capacitor assisted and diode assisted cascaded quasi-z-source inverters," *Electr. Rev.*, vol. 88, no. 1a, pp. 212–217, 2012.
[10] D. Vinnikov, I. Roasto, T. Jalakas, and S. Ott, "Extended boost quasi-z-source inverters: possibilities and challenges," *Electron. Electr. Eng.*, vol. 112, no. 6, pp. 51–56, 2011.
[11] V. Jagan, J. Kotturu, and S. Das, "Enhanced-boost quasi-z-source inverters with two-switched impedance networks," *IEEE Trans. Ind. Electron.*, vol. 64, no. 9, pp. 6885–6897, Sep. 2017.
[12] W. Qian, F. Z. Peng, and H. Cha, "Trans-z-source inverters," *IEEE Trans. Power Electron.*, vol. 26, no. 12, pp. 3453–3463, Dec. 2011.
[13] R. Strzelecki, M. Adamowicz, N. Strzelecka, and W. Bury, "New type T-source inverter," in *Proc. Compat. Power Electron.*, 2009, pp. 191–195.

[14] M. Adamowicz, "LCCT-z-source inverters," in *Proc. 10th Int. Conf. Environ. Electr. Eng.*, 2011, pp. 1–16.
[15] P. C. Loh, D. Li, and F. Blaabjerg, "Γ-Z-source inverters," *IEEE Trans. Power Electron.*, vol. 28, no. 11, pp. 4880–4884, Nov. 2013.
[16] M. -K. Nguyen, Y. -C. Lim, and Y. -G. Kim, "TZ-source inverters," *IEEE Trans. Ind. Electron.*, vol. 60, no. 12, pp. 5686–5695, Dec. 2013.
[17] Y. P. Siwakoti, P. C. Loh, F. Blaabjerg, and G. E. Town, "Y-source impedance network," *IEEE Trans. Power Electron.*, vol. 29, no. 7, pp. 3250–3254, Jul. 2014.
[18] R. R. Ahrabi and M. R. Banaei, "Improved Y-source DC–AC converter with continuous input current," *IET Power Electron*., vol. 9, no. 4, pp. 801–808, 2016.
[19] S. Asghari-Gorji, A. Mostaan, and H. Javadi, "A new structure of Y-source inverters with continous input current and high voltage gain," in *Proc. Power Electron., Drive Syst. Technol. Conf.*, 2015, pp. 515–520.
[20] M. Adamowicz and N. Strzelecka, "T-source inverter," *Electr. Rev.*, vol. 85, no. 10, pp. 233–238, 2009.
[21] M. -K. Nguyen, Y. -C. Lim, and S. -J. Park, "Improved trans-z-source inverter with continuous input current and boost inversion capability," *IEEE Trans. Power Electron.*, vol. 28, no. 10, pp. 4500–4510, Oct. 2013.
[22] Z. Aleem and M. Hanif, "Operational analysis of improved Γ-Z-Source inverter with clamping diode and its comparative evaluation," *IEEE Trans. Ind. Electron.*, vol. 64, no. 12, pp. 9191–9200, Dec. 2017.
[23] Q. Zhao and F. C. Lee, "High-efficiency, high step-up DC-DC converters," *IEEE Trans. Power Electron.*, vol. 28, no. 10, pp. 65–73, Jan. 2003.
[24] A. Hakemi, M. Sanatkar-Chayjani, M. Monfared, "Δ-Source Impedance Network," *IEEE Trans. Ind. Electron.*, vol. 64, no. 10, pp. 7842–7851, Oct. 2017.
[25] H. Wang and F. Blaabjerg, "Reliability of capacitors for DC-link applications in power electronic converters—An overview," *IEEE Trans. Ind. Appl.*, vol. 50, no. 5, pp. 3569–3578, Oct. 2014.
[26] MAGNETICS, *2017MPCC (2017) Magn. Powder Core Catalog*, 2017.
[27] International IAR Rectifier, *PD-20879 (2014) 30EPH06PbF Datasheet*, 2014.
[28] Y. S. Liu, B. M. Ge, and H. Abu-Rub, "An active power decoupling quasi-z-source cascaded multilevel inverter," in *Proc. Annu. Conf. IEEE Ind. Electron. Soc.*, 2016, pp. 6453–6458.
[29] Y. Ran, W. Wang, K. Liu, and H. P. Liu, "A power decoupling solution for improved single-phase Y-Source inverter," in *Proc. IETC Asia-Pacific*, 2017, pp. 1–5.

Hongpeng Liu (M'13) received the B.S. degree in electrical engineering from the Harbin University of Science and Technology, Harbin, China, in 2000, and the M.S. and Ph.D. degrees in electrical engineering from the Harbin Institute of Technology, Harbin, China, in 2006 and 2011, respectively.

In 2011, he joined Harbin Institute of Technology as an Assistant Professor with the Department of Electrical Engineering, where he has been an Associate Professor since December 2016. His current research interests include photovoltaic generation, microgrid, and PWM converter/inverter systems.

Zichao Zhou received the B.S. degree in electrical engineering from the Harbin Institute of Technology, Harbin, China, in 2017. He is currently working toward the M.S. degree in electrical engineering with the Harbin Institute of Technology.

His current research interests include photovoltaic generation and Y-source inverter.

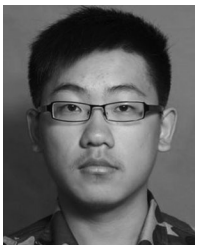

Kuan Liu received the B.S. degree in electrical engineering from the Harbin Institute of Technology, Harbin, China, in 2016. He is currently working toward the M.S. degree in electrical engineering with the Harbin Institute of Technology.

His current research interests include photovoltaic generation.

Poh Chiang Loh received the B.Eng (Hons.) and the M.Eng. degrees from the National University of Singapore, Singapore, in 1998 and 2000, respectively, and the Ph.D. degree from Monash University, Clayton, VIC, Australia, in 2002, all in electrical engineering.

His interests are in power converters and their grid applications.

Wei Wang (M'13) received the B.S. degree in automatic test and control from the Harbin Institute of Technology, Harbin, China, in 1984, the M.S. degree in electrical engineering from the Harbin Institute of Technology in 1990, and the Ph.D. degree in mechanical electronic engineering from the Harbin Institute of Technology in 2002.

In 1984, she joined the Harbin Institute of Technology, as an Assistant Professor with the Department of Electrical Engineering, where she was an Associate Professor from 1995 to 2003, and where she has been a Professor since 2003. Her current research interests include regenerative energy converter techniques, microgrid, soft-switching converters, and lighting electronic technology.

Dianguo Xu (M'97–SM'12–F'17) received the B.S. degree in control engineering from Harbin Engineering University, Harbin, China, in 1982, and the M.S. and Ph.D. degrees in electrical engineering from the Harbin Institute of Technology (HIT), Harbin, China, in 1984 and 1989 respectively.

In 1984, he joined the Department of Electrical Engineering, HIT as an Assistant Professor. Since 1994, he has been a Professor with the Department of Electrical Engineering, HIT. He was the Dean of School of Electrical Engineering and Automation, HIT from 2000 to 2010. He is currently the Vice President of HIT. His research interests include renewable energy generation technology, multiterminal HVDC system based on VSC, power quality mitigation, speed sensorless vector controlled motor drives, high-performance PMSM servo system. He published more than 600 technical papers.

Prof. Xu is an Associate Editor of the IEEE TRANSACTIONS ON INDUSTRIAL ELECTRONICS and the IEEE JOURNAL OF EMERGING AND SELECTED TOPICS IN POWER ELECTRONICS. He also serves as the Chairman of IEEE Harbin Section, Director of Lighting Power Supply Committee of CPSS, Vice-Director of Electric Automation Committee of CAA, Electrical Control System and Equipment Committee of CES, and Power Electronics Committee of CES.

Frede Blaabjerg (S'86–M'88–SM'97–F'03) received the Ph.D. degree from Aalborg University, Aalborg, Denmark, in 1992.

He was with ABB-Scandia, Randers, Denmark, from 1987 to 1988He became an Assistant Professor in 1992, Associate Professor in 1996, and Full Professor of power electronics and drives in 1998. His current research interests include power electronics and its applications such as in wind turbines, PV systems, reliability, harmonics and adjustable speed drives.

Dr. Blaabjerg has received 17 IEEE Prize Paper Awards, the IEEE PELS Distinguished Service Award in 2009, the EPE-PEMC Council Award in 2010, the IEEE William E. Newell Power Electronics Award 2014, and the Villum Kann Rasmussen Research Award 2014. He was an Editor-in-Chief of the IEEE TRANSACTIONS ON POWER ELECTRONICS from 2006 to 2012. He was nominated in 2014 and 2015 by Thomson Reuters to be among the most 250 cited researchers in engineering in the world.